Directive Surface Plasmons on Tunable Two-Dimensional Hyperbolic Metasurfaces and Black Phosphorus: Green's Function and Complex Plane Analysis

Seyyed Ali Hassani Gangaraj, *Student Member, IEEE*, Tony Low, Andrei Nemilentsau, and George W. Hanson, *Fellow, IEEE*

***Abstract*— We study the electromagnetic response of two- and quasi-two-dimensional (2-D) hyperbolic materials, on which a simple dipole source can excite a well-confined and tunable surface plasmon polariton (SPP). The analysis is based on the Green's function for an anisotropic 2-D surface, which nominally requires the evaluation of a 2-D Sommerfeld integral. We show that for the SPP contribution, this integral can be evaluated efficiently in a mixed continuous-discrete form as a continuous spectrum contribution (branch cut integral) of a residue term, in distinction to the isotropic case, where the SPP is simply given as a discrete residue term. The regime of strong SPP excitation is discussed, and the complex-plane singularities are identified, leading to physical insight into the excited SPP. We also present a stationary phase solution valid for large radial distances. Examples are presented using graphene strips to form a hyperbolic metasurface and thin-film black phosphorus. Green's function and complex-plane analysis developed allows for the exploration of hyperbolic plasmons in general 2-D materials.**

***Index Terms*— Anisotropy, complex plane analysis, directed surface plasmon, Green's function, hyperbolic surface.**

I. Introduction

RECENTLY, the development of nanofabrication technologies has made it possible to fabricate artificial materials exhibiting a hyperbolic regime—hyperbolic metamaterials (HMTMs) [1], [2]. HMTMs are uniaxial structures with extreme anisotropy, whose reactive effective material tensor components have the opposite signs for orthogonal electric field polarizations [3]. Hyperbolic materials exhibit hyperbolic, as opposed to the usual elliptic, dispersion, and combine the properties of transparent dielectrics and reflective metals [1]. These exotic properties have led to new physical phenomena and to the proposal for optical devices for a wide range of applications, such as far-field subwavelength imaging, nanolithography, emission engineering [1], negative index waveguides [4], subdiffraction photonic funnels [5], and nanoscale resonators [6].

The complexity of bulk fabrication of metamaterials has hindered the impact of this technology, especially in the optical regime, and volumetric effects may be detrimental to the associated losses [3]. Metasurfaces [7], [8], sheets of material with extreme subwavelength thickness, might address many of the present challenges and allow integration with planarized systems compatible with integrated circuits. Many high frequency electronics applications are envisioned for metasurfaces due to their ability to support and guide highly confined surface plasmons. The class of 2-D atomic crystals [9] represents the ultimate embodiment of a metasurface in terms of thinness, and often performance (e.g., tunability, flexibility, and quality factor). Some notable examples of 2-D layered crystals include graphene, transition metal dichalcogenides, trichalcogenides, black phosphorus (BP), boron nitride, and many more.

Graphene in particular has received considerable attention as a promising 2-D surface for many applications relating to large enhancement in Purcell emission, integrability, electronic tenability, and tranformation optics [10]–[17]. In addition to graphene, BP is also a layered material, with each layer forming a puckered surface due to sp^3 hybridization. It is one of the thermodynamically more stable phases of phosphorus, at ambient temperature and pressure [18]. BP has recently been exfoliated into its multilayers [19]–[22], showing good electrical transport properties. In particular, the optical absorption spectra of BP vary sensitively with thickness, doping, and light polarization, especially across the technologically relevant midinfrared to near-infrared spectrum [23]–[25]. Hence, it has also received considerable attention for optoelectronics, such as hyperspectral imaging and detection [26]–[29], photodetectors in silicon photonics [30], photoluminescence due to excitonic effects [31], and among many others.

Both natural materials and metasurfaces can be isotropic or anisotropic, and, e.g., isotropic graphene can be employed to form an effective anisotropic metasurface by modulating

Manuscript received September 1, 2015; September 8, 2016; accepted November 22, 2016. Date of publication December 1, 2016; date of current version March 1, 2017. The work of T. Low was supported by the MRSEC Program of the National Science Foundation under Award DMR-1420013.

S. A. Hassani Gangaraj and G. W. Hanson are with the Department of Electrical Engineering, University of Wisconsin-Milwaukee, Milwaukee, WI 53211 USA (e-mail: ali.gangaraj@gmail.com; george@uwm.edu).

T. Low is with the Department of Electrical and Computer Engineering, University of Minnesota, Minneapolis, MN 55455 USA (e-mail: tlow@umn.edu).

A. Nemilentsau was with the Department of Electrical Engineering, University of Wisconsin-Milwaukee, Milwaukee, WI 53211 USA. He is now with the Department of Electrical and Computer Engineering, University of Minnesota, Minneapolis, MN 55455 USA (e-mail: andrei.nemilentsau@gmail.com).

Color versions of one or more of the figures in this paper are available online at http://ieeexplore.ieee.org.

Digital Object Identifier 10.1109/TAP.2016.2633900

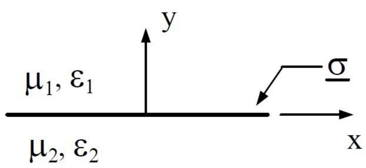

Fig. 1. Anisotropic surface with conductivity tensor $\overline{\sigma}$ at the interface of two isotropic materials.

its conductivity [3], [14]. In addition, both natural materials and metasurfaces may exhibit a hyperbolic regime. The basic properties of plasmons on 2-D hyperbolic surfaces have been recently studied: for metasurfaces comprised of anisotropic plasmonic particles in [32], for graphene strips in [3], and for general continuum 2-D materials including BP in [33].

In this paper, we provide Green's function for an anisotropic 2-D surface in the Sommerfeld integral form. We focus on complex-plane analysis of Green's function for the surface plasmon polariton (SPP) contribution in the hyperbolic case. The nominally 2-D Sommerfeld integral form of Green's function is very time-consuming to evaluate, and provides no physical insight into the resulting field. Here, we show that for the SPP field, this integral can be evaluated efficiently in a mixed continuous-discrete form as a continuous spectrum contribution (branch-cut integral) of a residue term. Complex-plane singularities are identified with various branch-cut integrals, leading to physical insight into the excited SPP. For some 2-D materials, the surface conductivity is rather weak, and a discussion is provided concerning the strength of the reactive conductivity response to maintain an SPP.

This paper is organized as follows. We discuss Green's function calculation for an anisotropic 2-D sheet with conductivity tensor $\underline{\sigma}$. A Hertzian dipole vertical current source serves as the excitation. Rigorous complex plane analysis is shown to reduce the 2-D iterated Sommerfeld integral to a residue for the inner integral (for the SPP contribution), and a branch cut for the outer integral [35]–[38]. The relevant singularities are detailed. We also provide a stationary phase (SP) evaluation leading to a closed-form solution for large radial distances. We show that graphene strips support propagation of directed surface waves and that the direction of propagation can be controlled by changing the frequency or doping. We also consider BP, which is dynamically tunable and anisotropic, and can be hyperbolic.

II. Fundamental Equations

The geometry under consideration is shown in Fig. 1. We consider an anisotropic layer with conductivity tensor

$$\underline{\sigma} = \begin{pmatrix} \sigma_{xx} & 0 \\ 0 & \sigma_{zz} \end{pmatrix} \tag{1}$$

embedded at the interface of two isotropic different materials with electrical properties ϵ_1 and μ_1 and ϵ_2 and μ_2.

For any planarly layered, piecewise-constant medium, the electric and magnetic fields in region n due to an electric current in any region are

$$\mathbf{E}^{(n)}(\mathbf{r}) = (k_n^2 + \nabla\nabla\cdot)\boldsymbol{\pi}^{(n)}(\mathbf{r}) \tag{2}$$

$$\mathbf{H}^{(n)}(\mathbf{r}) = i\omega\varepsilon_n \nabla \times \boldsymbol{\pi}^{(n)}(\mathbf{r}) \tag{3}$$

where $k_n = \omega(\mu_n\varepsilon_n)$ and $\pi^{(n)}(\mathbf{r})$ are the wavenumber and electric Hertzian potential in region n, respectively. The suppressed time convention is $e^{i\omega t}$. Assuming that the current source is in region 1, $\mathbf{J}^{(1)}$, then

$$\begin{aligned} \boldsymbol{\pi}^{(1)}(\mathbf{r}) &= \boldsymbol{\pi}_1^p(\mathbf{r}) + \boldsymbol{\pi}_1^s(\mathbf{r}) \\ &= \int_\Omega \{\underline{\mathbf{g}}^p(\mathbf{r},\mathbf{r}') + \underline{\mathbf{g}}^r(\mathbf{r},\mathbf{r}')\} \cdot \frac{\mathbf{J}^{(1)}(\mathbf{r}')}{i\omega\varepsilon_1}\, d\Omega' \\ \boldsymbol{\pi}^{(2)}(\mathbf{r}) &= \boldsymbol{\pi}_2^s(\mathbf{r}) = \int_\Omega \underline{\mathbf{g}}^t(\mathbf{r},\mathbf{r}') \cdot \frac{\mathbf{J}^{(1)}(\mathbf{r}')}{i\omega\varepsilon_1}\, d\Omega' \end{aligned} \tag{4}$$

where the underscore indicates a dyadic quantities, $\underline{\mathbf{g}}^p$ is the principal (free space) dyadic Green's function, $\underline{\mathbf{g}}^r$ is the reflected dyadic Green's function responsible for the fields in the region containing the source, $\underline{\mathbf{g}}^t$ is the transmitted dyadic Green's function responsible for the fields in the nonsource region (here, we assume a source in one region or the other, but not in both regions), and Ω is the support of the current. With y parallel to the interface normal, the principle Green's dyadic can be written as

$$\begin{aligned} \underline{\mathbf{g}}^p(\mathbf{r},\mathbf{r}') &= \underline{\mathbf{I}}\,\frac{e^{-ik_1R}}{4\pi R} \\ &= \underline{\mathbf{I}}\,\frac{1}{(2\pi)^2}\int_{-\infty}^{\infty}\int_{-\infty}^{\infty} \frac{e^{-p_1|y-y'|}}{2p_1} e^{-i\mathbf{q}\cdot(\mathbf{r}-\mathbf{r}')}\, dq_x dq_y \end{aligned} \tag{5}$$

where $\mathbf{q} = \widehat{\mathbf{x}}q_x + \widehat{\mathbf{z}}q_z$, $|\mathbf{q}| = q = (q_x^2+q_z^2)^{1/2}$, $p_n^2 = |\mathbf{q}|^2 - k_n^2$, $\rho = ((x-x')^2+(z-z')^2)^{1/2}$, $R = |\mathbf{r}-\mathbf{r}'| = (\rho^2+(y-y')^2)^{1/2}$, and $\underline{\mathbf{I}}$ is the unit dyadic.

The scattered (reflected or transmitted) Green's dyadics can be obtained by enforcing the boundary conditions

$$\begin{aligned} \widehat{\mathbf{z}} \times (\mathbf{H}_1 - \mathbf{H}_2) &= \mathbf{J}_e^s \\ \widehat{\mathbf{z}} \times (\mathbf{E}_1 - \mathbf{E}_2) &= -\mathbf{J}_m^s \end{aligned} \tag{6}$$

where $\mathbf{J}_e^s$ (A/m) and $\mathbf{J}_m^s$ (V/m) are electric and magnetic surface currents on the boundary. In our case, $\mathbf{J}_m^s = \mathbf{0}$, and $\mathbf{J}_e^s = \underline{\sigma}\cdot\mathbf{E}$. Using only an electric Hertzian potential, we can satisfy Maxwell's equations and the relevant boundary conditions. Introducing the 2-D Fourier transform

$$\mathbf{a}(\mathbf{q},y) = \int_{-\infty}^{\infty}\int_{-\infty}^{\infty} \mathbf{a}(\mathbf{r})e^{i\mathbf{q}\cdot\mathbf{r}}\, dxdz \tag{7}$$

$$\mathbf{a}(\mathbf{r}) = \frac{1}{(2\pi)^2}\int_{-\infty}^{\infty}\int_{-\infty}^{\infty} \mathbf{a}(\mathbf{q},y)e^{-i\mathbf{q}\cdot\mathbf{r}}\, dq_x dq_z \tag{8}$$

and enforcing the boundary conditions, the scattered Green's dyadic is found to have the form

$$\underline{\mathbf{g}}^{r,t} = \begin{pmatrix} g_{xx}^{r,t} & g_{xy}^{r,t} & 0 \\ g_{yx}^{r,t} & g_{yy}^{r,t} & g_{yz}^{r,t} \\ 0 & g_{zy}^{r,t} & g_{zz}^{r,t} \end{pmatrix} \tag{9}$$

where the Sommerfeld integrals are

$$\begin{aligned} &g_{\alpha\beta}^r(\mathbf{r},\mathbf{r}') \\ &= \frac{1}{(2\pi)^2}\int_{-\infty}^{\infty}\int_{-\infty}^{\infty} w_{\alpha\beta}^r(q_x,q_z)\frac{e^{-p_1(y+y')}}{2p_1} e^{-i\mathbf{q}\cdot(\mathbf{r}-\mathbf{r}')}\, dq_x dq_z. \end{aligned} \tag{10}$$

Green's dyadic for region 2, $\underline{\mathbf{g}}^t(\mathbf{r}, \mathbf{r}')$, has the same form as for region 1, although in (10), the replacement $w^r_{\alpha\beta} e^{-p_1(y+y')} \to w^t_{\alpha\beta} e^{p_2 y} e^{-p_1 y'}$ must be made.

The coefficients $w^{r,t}_{\alpha\beta}$ are complicated for the inhomogeneous case, and so for simplicity in the following, we assume that the sheet is in a homogeneous space $\varepsilon_2 = \varepsilon_1 = \varepsilon$, $\mu_2 = \mu_1 = \mu$. When region 2 differs from region 1, the only change is in the functions (11) and (12) provided in the following. Concentrating on the field in the upper half-space, $w^r_{\alpha\beta} = N_{\alpha\beta}(q_x, q_z)/D(q_x, q_z)$, where

$$D(q_x, q_z) = 2\sigma_{xx}(k^2 - q_x^2) + 2\sigma_{zz}(k^2 - q_z^2) - i4\frac{k}{\eta} p\left(1 + \frac{1}{4}\eta^2 \sigma_{xx}\sigma_{zz}\right) \tag{11}$$

and

$$\begin{aligned} N_{yy}(q_x, q_z) &= -p^2(\sigma_{xx} + \sigma_{zz}) - ipk\eta\sigma_{xx}\sigma_{zz} \\ N_{xy}(q_x, q_z) &= iq_x p(\sigma_{xx} - \sigma_{zz}) \\ N_{zy}(q_x, q_z) &= -iq_z p(\sigma_{xx} - \sigma_{zz}) \end{aligned} \tag{12}$$

where $p = (q_x^2 + q_z^2 - k^2)^{1/2}$, and $\eta = (\mu/\varepsilon)^{1/2}$. Then, e.g., for the vertical field in the upper half-space

$$E_y = \frac{1}{i\omega\epsilon}\left(k^2 + \frac{\partial^2}{\partial y^2}\right)(g^p_{yy}(\mathbf{r}, \mathbf{r}') + g^r_{yy}(\mathbf{r}, \mathbf{r}')) + \frac{1}{i\omega\epsilon}\left(\frac{\partial^2}{\partial x \partial y} g^r_{xy}(\mathbf{r}, \mathbf{r}') + \frac{\partial^2}{\partial z \partial y} g^r_{zy}(\mathbf{r}, \mathbf{r}')\right) \tag{13}$$

and other field components are obtained from (2).

III. Directional Properties of SPPs on 2-D Surfaces

Before considering complex-plane evaluation of Green's functions, we describe some basic properties of SPPs on hyperbolic 2-D surfaces [3], [32], [33]. In order to understand the behavior of surface waves, it is instructive to inspect the plasmon dispersion relation $D(q_x, q_z) = 0$ arising from (11), the denominator of Green's function. As we show later, in the general case, SPPs are obtained as a mixture of TE and TM modes, and moreover, it is not possible to solve for the wave vector eigenmodes q_x and q_z from the single complex-valued equation (11). Furthermore, unlike for isotropic surfaces, for an anisotropic medium, the direction of energy transfer is defined by the group velocity in the medium [34] $\nabla_{\mathbf{q}}\omega(\mathbf{q})$, and does not coincide with the direction of the plasmon wave vector $\mathbf{q}$. In our case, the dispersion relation for surface plasmons is complicated and the group velocity cannot be calculated analytically. However, we can estimate the direction of plasmon propagation geometrically by examining the plasmon's equifrequency contours, $\omega(\mathbf{q}) = \text{const}$. As the group velocity is a gradient of frequency with respect to wave vector, the direction of plasmon energy flow is necessary orthogonal to the equifrequency contours.

Assuming that the conductivity is purely imaginary and lossless, $\sigma_{jj} = i\sigma''_{jj}$, $j = x, z$, and that $q_x, q_z \gg k$, the zeros of (11) can be approximated as the solution of

$$\frac{q_x^2}{\sigma''_{zz}} + \frac{q_z^2}{\sigma''_{xx}} = 2p\omega\left(\frac{\varepsilon_0}{\sigma''_{xx}\sigma''_{zz}} - \frac{\mu_0}{4}\right). \tag{14}$$

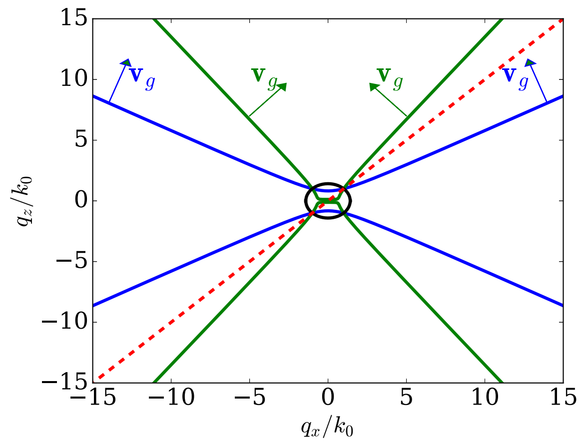

Fig. 2. Equifrequency surfaces for metasurface having $\sigma_{xx} = 0.003 + 0.25i$ mS and $\sigma_{zz} = 0.03 - 0.76i$ mS [blue hyperbola, see also Fig. 10(b)], and $\sigma_{xx} = 1.3 + 16.9i$ mS and $\sigma_{zz} = 0.4 - 9.2i$ mS [green hyperbola, see also Fig. 10(c)]. For comparison, the isotropic case for $\sigma_{xx} = \sigma_{zz} = 0.03 - 0.76i$ mS (black circle) is also shown. Red dashed line: 45° with respect to the x-axis for guidance.

Although the right side varies with $\mathbf{q}$ because of the square root p, the variation is less than the left side, and we can approximate the right side as being constant in wavenumber. Then, in the hyperbolic case ($\sigma''_{xx} \cdot \sigma''_{zz} < 0$), the equifrequency surface (EFS) is a hyperbola, as shown in Fig. 2 for two values of surface conductivity [blue lines: $\sigma_{xx} = 0.003 + 0.25i$ mS and $\sigma_{zz} = 0.03 - 0.76i$ mS, see also Fig. 10(b), and green lines: $\sigma_{xx} = 1.3 + 16.9i$ mS and $\sigma_{zz} = 0.4 - 9.2i$ mS, see also Fig. 10(c)]; the results in Fig. 2 were obtained by the solution of the full dispersion relation (11). The hyperbola asymptotes are defined by $q_z = \pm q_x(|\sigma''_{xx}/\sigma''_{zz}|)^{1/2}$. Taking into account that a dipole excites many plasmons with different values of $\mathbf{q}$, and that the normal to all the points on the hyperbola point in the same direction for a given sign of q_x, we expect a narrow plasmon beam in the direction of energy flow on a hyperbolic metasurface. For example, the asymptotes of the blue hyperbola in Fig. 2 have an angle 30° with respect to the x-axis, and thus, the normal to the hyperbola, i.e., the group velocity, is 60° with respect to the x-axis, as indicated in the figure, which is in a very good agreement with the numerical results shown in Fig. 10(b). Similar comments apply to the green hyperbola and Fig. 10(c). For comparison, in Fig. 2, we also presented the hypothetical isotropic case for which the equifrequency contour is a circle, and thus, energy does not have a preferential direction.

In the nonhyperbolic (purely anisotropic) case ($\sigma''_{xx}, \sigma''_{zz} > 0$), (14) is the equation for an ellipse in $\mathbf{q}$-space with the axis oriented along the q_x-axis and the q_z-axis. The length of the ellipse's principal axes along the q_x-axis and the q_z-axis is proportional to σ''_{zz} and σ''_{xx}, respectively. Thus, the EFS has a quasi-eliptic form elongated along the direction of the smallest component of the conductivity tensor, the degree of elongation being set by the ratio of σ''_{xx} and σ''_{zz}. Later, in Fig. 11, we consider BP having $\sigma_{xx} = 0.0008 - 0.2923i$ mS and $\sigma_{zz} = 0.0002 - 0.0658i$ mS. Due to the strong elongation of the EFS along the q_z-axis, the group velocity points approximately along the q_x-axis, such that the SPP carries energy along the x crystallographic axis (see Fig. 11).

IV. Complex-Plane Analysis in the q_x Plane

In the case of an isotropic material, the coefficients $w_{\alpha\beta}$ only depend on $q^2 = q_x^2 + q_z^2$, leading to

$$\begin{aligned} g^r_{\alpha\beta}(\mathbf{r}, \mathbf{r}') &= \frac{1}{2\pi}\int_0^\infty w_{\alpha\beta}(q)\frac{e^{-p(y+y')}}{2p}J_0(q\rho)q\,dq \\ &= \frac{1}{2\pi}\int_{-\infty}^\infty w_{\alpha\beta}(q)\frac{e^{-p(y+y')}}{4p}H_0^{(2)}(q\rho)q\,dq \end{aligned} \quad (15)$$

where J_0 and $H_0^{(2)}$ are the usual zeroth-order Bessel and Hankel functions, respectively. These two forms can be converted one into another using the relation $J_0(\alpha) = (1/2)[H_0^{(1)}(\alpha) + H_0^{(2)}(\alpha)]$, $H_0^{(2)}(-\alpha) = -H_0^{(1)}(\alpha)$. In this case, such as occurs for graphene without a magnetic bias, the pole of $w_{\alpha\beta}$ leads to a simple analytical form for the SPP field [12]. However, this is not the case for an anisotropic surface. Since the 2-D Sommerfeld integral can be time-consuming to evaluate, writing

$$g^r_{\alpha\beta}(\mathbf{r}, \mathbf{r}') = \frac{1}{(2\pi)}\int_{-\infty}^\infty dq_z e^{-iq_z(z-z')}f_{\alpha\beta}(q_z) \quad (16)$$

where

$$f_{\alpha\beta}(q_z) = \frac{1}{(2\pi)}\int_{-\infty}^\infty w_{\alpha\beta}(q_x, q_z)\frac{e^{-p(y+y')}}{2p}e^{-iq_x(x-x')}dq_x \quad (17)$$

the "inner" integral $f_{\alpha\beta}(q_z)$ can be evaluated as an SPP residue term (discrete spectral component) and branch-cut integral representing the radiation continuum into space (note that the choice of "inner" and "outer" integrals is arbitrary). The branch cut in the q_x plane is the usual hyperbolic branch cut associated with the branch point due to $p = (q_x^2 + q_z^2 - k^2)^{1/2}$, occurring at $q_x = \pm(k^2 - q_z^2)^{1/2}$ [39]. Then

$$\begin{aligned} f_{\alpha\beta}(q_z) &= -i\,w^{\text{spp}}_{\alpha\beta}(q_{xp}, q_z)\frac{e^{-p(q_{xp})(y+y')}}{2p(q_{xp})}e^{-iq_{xp}(x-x')} \\ &\quad + \frac{1}{2\pi}\int_{\text{bc}} w_{\alpha\beta}(q_x, q_z)\frac{e^{-p(y+y')}}{2p}e^{-iq_x(x-x')}dq_x \end{aligned} \quad (18)$$

where the first term is the residue contribution and bc indicates the hyperbolic branch-cut contour. In (18), $w^{\text{spp}}(q_{xp}, q_z) = N(q_{xp}, q_z)/D'(q_{xp}, q_z)$, $D'(q_x, q_z) = (\partial/\partial q_x)D(q_x, q_z)$, and where q_{xp} is the root of $D(q_x, q_z) = 0$ for a given q_z

$$q_{xp}(q_z) = \pm\sqrt{\frac{-B \pm \sqrt{B^2 - 4AC}}{2A}} \quad (19)$$

where $A = \sigma_{xx}^2$, $B = (1/4)\alpha^2 - 2k^2\sigma_{xx}^2 + 2(q_z^2 - k^2)\sigma_{xx}\sigma_{zz}$, $C = k^4(\sigma_{xx} + \sigma_{zz})^2 + q_z^2(q_z^2 - 2k^2)\sigma_{zz}^2 - 2k^2q_z^2\sigma_{xx}\sigma_{zz} + (1/4)\alpha^2(q_z^2 - k^2)$, and $\alpha = (4k/\eta)(1 + (1/4)\eta^2\sigma_{xx}\sigma_{zz})$.

When the SPP field is the dominant contribution to the response, which is the usual regime for plasmonics where the field close to the interface, $(y, y' \ll \lambda)$) is of interest, the branch-cut term can be ignored, and the residue term suffices for the calculation of $f(q_z)$

$$f^{\text{SPP}}_{\alpha\beta}(q_z) \approx -i\,w^{\text{spp}}_{\alpha\beta}(q_{xp}, q_z)\frac{e^{-p(q_{xp})(y+y')}}{2p(q_{xp})}e^{-iq_{xp}(x-x')} \quad (20)$$

which considerably speeds up evaluation of Green's function (rendering it 1-D). Since q_{xp} is the propagation constant along the x-axis, the $\mp$ outside the square root in (19) indicates forward/backward propagation, whereas the inner $\pm$ sign choice governs propagation of different modes (only one of which will propagate). Assuming $(x - x') > 0$, the term $e^{-iq_{xp}(x-x')}$ necessitates that $\text{Im}(q_{xp}) < 0$ to have a decaying wave traveling away from the source along the x-axis.

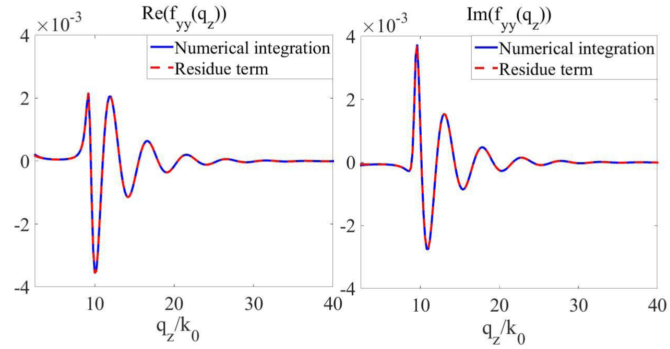

Fig. 3. Real and imaginary parts of $f_{yy}(q_z)$ obtained numerically, (17), and using the residue term (20) for an array of graphene strips at $f = 10$ THz. The source is $\lambda/50$ above the surface, and $x = 0.2\lambda$.

As an example, we consider an anisotropic surface with $\sigma_{xx} = 0.02 + 0.57i$ mS and $\sigma_{zz} = 0.02 - 0.57i$ mS. As discussed in Appendix A, such a conductivity tensor can be physically realized by an array of densely packed graphene strips at terahertz and near-infrared frequencies. Fig. 3 compares $f_{yy}(q_z)$ obtained numerically by performing the integral (16) and obtained by using the residue term only [see (20)]. The source is located at $y' = \lambda/50$, very near the surface, and radiating at frequency 10 THz. Clearly, in the SPP regime, the residue provides the dominant component of the response, and the branch-cut integral can be ignored. Although not shown, for source or observation points relatively far from the surface, the branch-cut integral is important, and can be the dominant contribution to the scattered field.

In the following, we are interested in surfaces that provide a strong reactive and low-loss response, $\text{Im}(\sigma_{\alpha\alpha}) \gg \text{Re}(\sigma_{\alpha\alpha})$. In addition to this inequality, $\text{Im}(\sigma_{\alpha\alpha})$ must not be too small [40]. The ability of a surface to support a strong SPP depends on the ratio of the branch cut term (space radiation spectra) to the residue (SPP) term in the inner integral (18). In Fig. 4, we assume a general hyperbolic form $\sigma_{xx} = \alpha\sigma_0(0.01 + i)$ and $\sigma_{zz} = 0.1\sigma_{xx}^*$, where $\sigma_0 = e^2/4\hbar$ is the conductance quantum, e is the electron charge, and $*$ indicates complex conjugation. We assume that losses are relatively small, and use α in order to vary the magnitude of the conductivity.

It is clearly shown in Fig. 4 that for conductivity values smaller than the conductance quantum, the radiation spectra is dominant (in the limit that $|\sigma| \to 0$, the surface vanishes

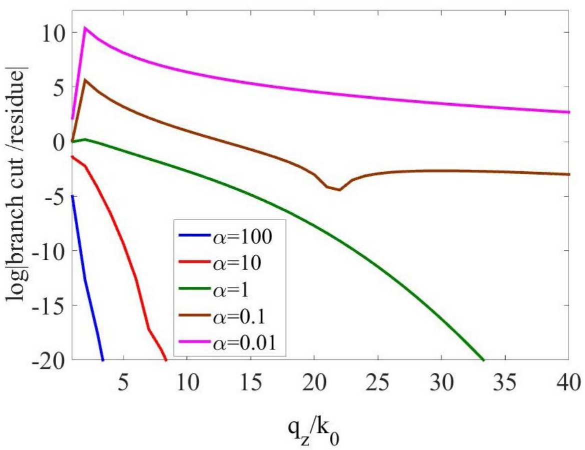

Fig. 4. Ratio of the branch cut and residue terms in (18), $\sigma_{xx} = \alpha\sigma_0(0.01+i)$, $\sigma_{zz} = 0.1\sigma_{xx}^*$, and $\sigma_0 = e^2/4\hbar$. Source is positioned $\lambda/50$ above the surface, $f = 10$ THz, and $x = 0.2\lambda$.

and the entire response is the radiation continuum produced by a source in free space). We have found that conductivity values on the order of the conductance quantum are somewhat borderline; an SPP can exist, although it may not be strongly dominant over the branch-cut continuum for small q_z. Conductivities an order of magnitude or more above the conductance quantum provide a very strong SPP response in which the branch-cut contribution is negligible except exceedingly close to the source.

For large q_z compared with k, (19) becomes

$$q_{xp}(q_z) = q_z\sqrt{-\frac{\sigma_{zz}}{\sigma_{xx}}}. \tag{21}$$

The SPP direction of propagation on the 2-D anisotropic surface is easily determined as $\tan^{-1}(q_{xp}/q_z)$, and using (21), the angle of propagation with respect to the z-axis is simply

$$\phi = \tan^{-1}\sqrt{-\frac{\sigma''_{zz}}{\sigma''_{xx}}} \tag{22}$$

where $\sigma'' = \mathrm{Im}(\sigma)$. Although the conductivities are complex-valued, for the low-loss cases of interest, we can estimate the real angle ϕ by only considering their imaginary parts. Therefore, in the anisotropic hyperbolic case, the SPP is directed along a specific angle. For the isotropic case ($\sigma_{xx} = \sigma_{zz}$), this does not occur [and (22) does not apply], since in this case, $q_{xp}^2 + q_z^2 = q_p^2$, where q_p is the radial in-plane wavenumber. If we measure the angle ϕ relative to the positive z-axis, then at each point in the plane of the surface, we have $x = \rho\sin\phi$, $z = \rho\cos\phi$, $q_{xp} = q_p\sin\phi$, and $q_z = q_p\cos\phi$. For a source at the origin

$$e^{-i\mathbf{q}\cdot(\mathbf{r}-\mathbf{r}')} = e^{-i(q_{xp}x+q_z z)} = e^{-iq_p\rho(\cos^2\phi+\sin^2\phi)} = e^{-iq_p\rho} \tag{23}$$

which $e^{-iq_p\rho}$ describes an SPP wave that is radially propagating along all directions in the plane of the surface. However, in the anisotropic case for large q_z

$$\begin{aligned} e^{-i\mathbf{q}\cdot(\mathbf{r}-\mathbf{r}')} &= e^{-i(q_{xp}x+q_z z)} = e^{-i\left(q_z\sqrt{-\frac{\sigma_{zz}}{\sigma_{xx}}}x+q_z z\right)} \\ &= e^{-iq_z\rho\left(\sqrt{-\frac{\sigma_{zz}}{\sigma_{xx}}}\sin\phi+\cos\phi\right)} \end{aligned} \tag{24}$$

and the maximum of $((-(\sigma_{zz}/\sigma_{xx}))^{1/2}\sin\phi + \cos\phi)$ determines the angle at which the SPP is directed. It can be simply shown that this angle is (22). This leads to the conclusion that hyperbolic anisotropy, in contrast to the isotropic case, results in a directed SPP, as expected.

As a function of $\underline{\sigma}$, there are different dispersion scenarios for SPP propagation. The usual elliptic case is obtained when both imaginary parts of the conductivity have the same sign (inductive when $\mathrm{Im}(\sigma_{xx,zz}) < 0$, capacitive otherwise). A graphene sheet with dominant intraband conductivity term with $\mathrm{Im}(\sigma_{xx}) = \mathrm{Im}(\sigma_{zz}) < 0$ is a natural example of an elliptic isotropic sheet that can support a TM omnidirectional SPP. The hyperbolic case occurs when the sign of the imaginary parts of the conductivity components is different. As discussed in Appendixes A and B, both a graphene strip metasurface (potentially, metal strips as well) and natural BP can provide a hyperbolic 2-D surface. In this case, as shown in (22) and (24), energy propagation is focused along the specific directions governed by the conductivity components [3].

V. Approximation of the Outer Integral Using Stationary Phase and Exact Evaluation Using the Continuous Spectrum

Although the SPP field can be evaluated from a numerical 1-D integral, (16) with (20), it is useful to consider other methods of evaluation that are more computationally rapid, and which lead to physical insight into the problem.

A. Stationary Phase Evaluation of the Outer Integral

The "outer" integral (16) using (20) can be approximated by the well-known method of SP [41]. In particular, an analysis similar to that needed here was performed in [42], where the inner integral is approximated as a residue (ignoring the branch-cut contribution, as we do here), and the outer integral is evaluated using SP. Regarding computation of the outer integral, although it seems difficult to show analytically because of the complicated expression (19) for the pole $q_{xp}(q_z)$, the numerical tests show that $\mathrm{Re}(q_{xp}^2 + q_z^2 - k^2) > 0$ for small values of q_z. Therefore, no leaky waves are encountered for typical parameter values.

SP evaluation of (16) with (20), assuming $\rho \gg (y + y')$, results in, to the first order

$$g^r_{\alpha\beta}(\mathbf{r},\mathbf{r}') \simeq \sqrt{\frac{e^{-i\frac{\pi}{2}}}{2\pi\gamma''(q_s)}}\, w^{\mathrm{spp}}_{\alpha\beta}(q_s)\frac{e^{-p(q_s)(y+y')}}{2p(q_s)}\, e^{-i\gamma(q_s)} \tag{25}$$

where $w^{\mathrm{spp}}_{\alpha\beta}(q_s) = w^{\mathrm{spp}}_{\alpha\beta}(q_{xp}(q_s), q_s)$, $p(q_s) = p(q_{xp}(q_s), q_s)$, and $\gamma(q_z) = -(q_{xp}(q_z)(x - x') + q_z(z - z'))$, where q_s is the root of $d\gamma/dq_z = 0$, which can be obtained as the root of a fourth-order polynomial, or via numerical root search. See [42] for a ray-optical interpretation of the SP result in anisotropic media.

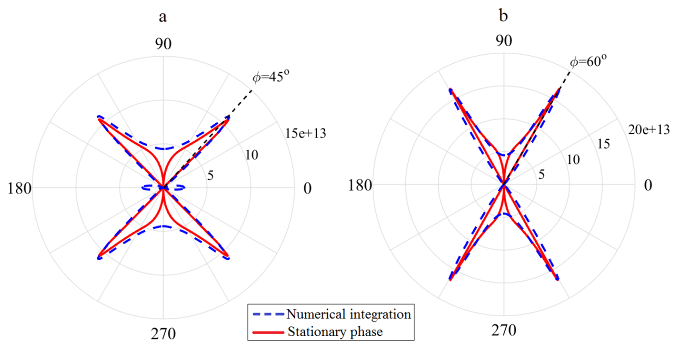

Fig. 5. Electric field E_y obtained by SP result (25) (red) and numerical integration (16) (blue) for (a) $\sigma_{xx} = 0.02 + 0.57i$ mS and $\sigma_{zz} = 0.02 - 0.57i$ mS and (b) $\sigma_{xx} = 0.003 + 0.25i$ mS, $\sigma_{zz} = 0.03 - 0.76i$ mS, $\rho = 0.4\lambda$, $\rho/(y + y') = 80$, and $f = 10$ THz.

Although the main numerical results will be presented in Section VI, here we provide a comparison between the SP result (25) and numerical (real-line) computation of the outer integral (16). Fig. 5 shows the SP result (red) and numerical integration result (blue) for $\sigma_{xx} = 0.02 + 0.57i$ mS and $\sigma_{zz} = 0.02 - 0.57i$ mS and $\sigma_{xx} = 0.003 + 0.25i$ mS and $\sigma_{zz} = 0.03 - 0.76i$ mS, both using $\rho = 0.4\lambda$, $\rho/(y + y') = 80$. It can be seen that excellent agreement is found for the location of the beam angle, although away from the beam maximum, there is some disagreement.

B. Complex-Plane Analysis in the q_z Plane

Although the SPP field can be evaluated to first-order using the SP approximation for $\rho/(y + y') \gg 1$, it is useful to consider complex-plane analysis of the "outer" integral over q_z, which turns out to involve only continuous spectrum. This method is theoretically exact, and is valid for all field and source points. Furthermore, it does not require finding the q_z root, but does require knowing the q_z plane branch points and cuts, which, themselves, lead to considerable physical insight.

The Weierstrass preparation theorem shows that the complex function $f_{\alpha\beta}^{\mathrm{SPP}}(q_z)$, (20), has no poles, only branch points. Regarding the two complex planes $q_x - q_z$, a sufficient condition in order to have a branch point in the q_z is that [43], [44]

$$D(q_x, q_z) = \frac{\partial}{\partial q_x} D(q_x, q_z) = 0 \tag{26}$$

with $\delta = (\partial/\partial q_z) D(q_x, q_z)(\partial^2/\partial q_x^2) D(q_x, q_z) \neq 0$. Although (26) represents a second-order zero of D, in the q_z-plane, these points are not poles, and are also not necessarily q_z plane branch points without the condition $\delta \neq 0$. These branch points are associated with modes in the q_x plane merging at a certain value of q_z, forming a second-order zero of D. Thus, the pair (q_x, q_z) satisfying (26) and $\delta \neq 0$ represent poles in the q_x plane and branch points in the q_z plane (the branch in the q_z plane controls the merging of poles in the q_x plane). Another possible branch point in the q_z plane is associated with the square root in p. The fact that a pole in one spectral plane results in a branch point in another spectral plane was recognized in studies of microstrip and other integrated waveguides [35]–[38]. It is also worthwhile to note that the asymptotic methods for branch-cut evaluation described in [41] do not work here. To use those formulas, the branch-cut integral must be dominated by the branch point, that is, by the section of the integral in the vicinity of the branch point. This is not the case for the anisotropic problem, where we have found that the sections of the branch-cut integral far from the branch point can contribute substantially.

C. p-Type Branch Point in the q_z plane

For the isotropic case, $p = (q^2 - k^2)^{1/2}$ and the p-type branch point occurs at $q = \pm k$, resulting in the usual hyperbolic branch cuts in the q plane [39]. In this case, $q_x^2 + q_z^2 = q_p^2$ is a constant and $q_z = (k^2 - q_x^2)^{1/2}$ leads to branch points at $q_x = \pm k$. However, for the residue, $q_p^2 = q_{xp}^2(q_z) + q_z^2$ is a constant in q_z and so we never have $q_p = k$ for any q_z, and so there is no p-type BP in the q_z plane for the SPP for the isotropic case. However, for anisotropic media, $q_{xp}^2(q_z) + q_z^2$ is not generally a constant, and so there can be a "p-type" BP in the q_z-plane, where $p = (q_{xp}^2(q_z) + q_z^2 - k^2)^{1/2} = 0$, although this will not occur at $q_z = k$ unless $q_{xp}(k) = 0$. In any event, since this branch cut relates to radiation into space, for the SPP, we can ignore this contribution to the SPP field.

Introducing the notation that $(q_x^{(n)}, q_z^{(n)})$ represents the pair of spectral values that satisfy the conditions for a branch point/pole pair, (26) and $\delta \neq 0$, since the residue term already satisfies $D(q_{xp}, q_z) = 0$, and we can find branch points in the q_z plane from $\frac{\partial}{\partial q_x} D(q_{xp}(q_z), q_z) = 0$

$$\left(\sigma_{xx} + \frac{ik/\eta}{\sqrt{q_{xp}^2 + q_z^2 - k^2}}\left(1 + \frac{1}{4}\eta^2\sigma_{xx}\sigma_{zz}\right)\right) q_{xp}(q_z) = 0. \tag{27}$$

As we will show later, these branch points have a significant role in the analysis of the SPP. Because of their importance, we categorize them into two groups, type-0 and type-1 branch points.

D. Type-0 Branch Point in the q_z Plane

First, we define type-0 branch points as those values of q_z for which $q_{xp}(q_z) = 0$ in (27), i.e., the merging of the forward and backward modes [associated with different signs in the outer square root in (19)] in the q_x plane at a certain value of q_z [44], given by

$$q^{(+0)} = q_z^{\mathrm{TM}} = k\sqrt{1 - \left(\frac{2}{\eta\sigma_{zz}}\right)^2} \tag{28}$$

$$q^{(-0)} = q_z^{\mathrm{TE}} = k\sqrt{1 - \left(\frac{\eta\sigma_{xx}}{2}\right)^2} \tag{29}$$

such that the pair $(q_x, q_z) = (0, q^{\mathrm{TM/TE}})$ form a pole-branch-point pair. For $\sigma_{xx} = \sigma_{zz}$, these are well-known TM and TE SPP wavenumbers, respectively (graphene is an example of such a 2-D isotropic layer, which can support these modes [12]). Note that for isotropic media, a vertically polarized current source will produce only TM fields (although a horizontally polarized source will produce both TE and TM fields even when the sheet is isotropic [39]). For an anisotropic sheet, the boundary conditions cannot be satisfied assuming only one type of field.

E. Type-1 Branch Point in the q_z Plane

Another set of singularities in the q_x–q_z plane is related to the point in the q_z plane where modes q_{xp} associated with different signs in the inner square root in (19) merge for $q_{xp} \neq 0$. These can be obtained by simultaneously solving the equations $D(q_x, q_z) = 0$ and $(dD(q_x, q_z)/dq_x) = 0$, leading to

$$q_x^{(\pm 1)} = \sqrt{\frac{-k^2}{\delta\sigma}\left(\sigma_{xx} + (\sigma_{zz} \mp 2\sigma_{xx})\frac{(1+\frac{1}{4}\eta^2\sigma_{xx}\sigma_{zz})^2}{\eta^2\sigma_{xx}^2}\right)} \tag{30}$$

$$q_z^{(\pm 1)} = \sqrt{-(q_x^{(\pm 1)})^2 + k^2\left(1 - \frac{\left(1+\frac{1}{4}\eta^2\sigma_{xx}\sigma_{zz}\right)^2}{\eta^2\sigma_{xx}^2}\right)} \tag{31}$$

where $\delta\sigma = \sigma_{zz} - \sigma_{xx}$, such that $(q_x, q_z) = (q_x^{(\pm 1)}, q_z^{(\pm 1)})$ forms a pole-branch-point pair.

F. Branch-Cut Analysis in the q_z Plane

Using the SPP field (20) and performing the outer integration, Green's function is

$$g^r_{\alpha\beta} = \frac{-i}{2\pi}\int_{-\infty}^{+\infty} w'_{\alpha\beta}(q_{xp}, q_z)\frac{e^{-p(y+y')}}{2p}e^{-iq_{xp}(x-x')} \times e^{-iq_z(z-z')}dq_z. \tag{32}$$

Assuming $(z-z') > 0$, due to the term $e^{-iq_z(z-z')}$, the contour can be closed in the lower half-plane of the q_z plane, leading to

$$g^r_{\alpha\beta} \approx \frac{-i}{2\pi}\int_{\mathrm{bc}} w'_{\alpha\beta}(q_{xp}, q_z)\frac{e^{-p(y+y')}}{2p}e^{-iq_{xp}(x-x')} \times e^{-iq_z(z-z')}dq_z \tag{33}$$

where the branch-cut integral is over all branch cuts. Also, from the term $e^{-iq_{xp}(x-x')}$, it is clear that for $x - x' \gtrless 0$ then only when $\mathrm{Im}(q_{xp}) \lesseqgtr 0$ do we obtain an SPP that decays away from the source. Therefore, we have in the q_z plane two Riemann sheets (as mentioned previously, neglecting the p-type branch point, which would introduce another two sheets; here, we simply enforce $\mathrm{Re}(p) > 0$), the top (proper) sheet where $\mathrm{Im}(q_{xp}) \lesseqgtr 0$ and the bottom sheet where $\mathrm{Im}(q_{xp}) \gtrless 0$, for $x - x' \gtrless 0$. Those values of q_z that lead to $\mathrm{Im}(q_{xp}) = 0$ determine the branch-cut trajectory, which separates the proper from improper Riemann sheets.

Typically, branch-cut trajectories to separate certain Riemann sheets can be analytically determined from the functional dependence of the multivalued function that defines the branch point. However, for anisotropic surfaces, the form of q_{xp} is too complicated to determine a simple equation for the branch cut for $\mathrm{Im}(q_{xp}) = 0$. As an example,

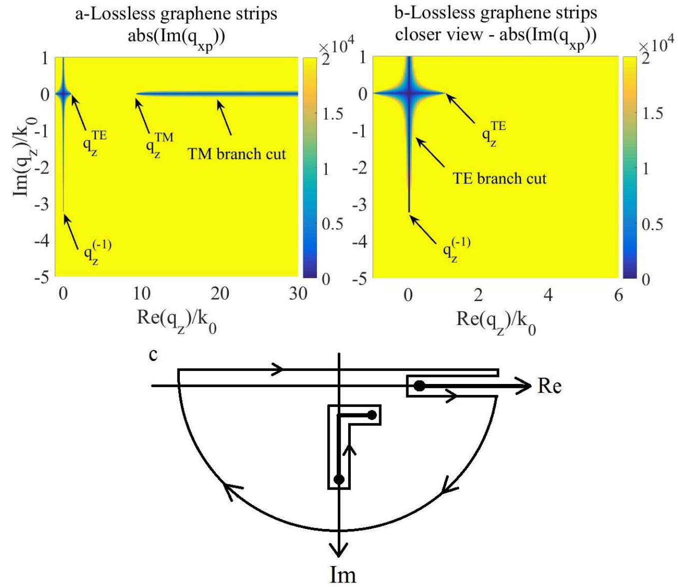

Fig. 6. (a) and (b) Branch-cut contours $\mathrm{Im}(q_{xp}) = 0$ determined from a plot of the absolute value of $\mathrm{Im}(q_{xp})$ for a lossless model of a graphene strip array at 10 THz ($\sigma'_{xx} = \sigma'_{zz} = 0$, $\sigma''_{xx} = 0.57i$ mS, and $\sigma''_{zz} = -0.57i$ mS). The branch point locations are $q_z^{\mathrm{TE}}/k = 1.005$, $q_z^{\mathrm{TM}}/k = 9.3$, and $q_z^{(-1)}/k = -3.22i$. (c) Integration contour in the q_z plane showing branch points (dots) and branch cuts (thick lines).

Fig. 6(a) shows the branch cuts for $\mathrm{Im}(q_{xp}) = 0$ obtained by plotting $\mathrm{Im}(q_{xp})$ for an array of graphene strips (see Appendix A) in the hypothetical lossless case (i.e., ignoring the real parts of the conductivities) at 10 THz. Fig. 6(b) shows a close-up near the Im-axis, and Fig. 6(c) shows the properly cut q_z plane for the lossless case. It can be seen that for the considered frequency, the TM branch point leads to a branch cut starting at q_z^{TM} and going horizontally to infinity, and the TE branch point q_z^{TE} and the branch point $q_z^{(-1)}$ are connected by a branch cut. The branch point $q_z^{(+1)}$ is on the improper Riemann sheet (not shown).

Insight into the correct branch cut can be obtained from a large q_z approximation. From (21), for a lossy 2-D surface, $\sigma_{xx} = \sigma'_{xx} + i\sigma''_{xx}$ and $\sigma_{zz} = \sigma'_{zz} + i\sigma''_{zz}$, and then, the branch cut trajectory is along the q_z values such that

$$\mathrm{Im}\left(iq_z\sqrt{\sigma'_{zz}\sigma'_{xx} + i\sigma''_{zz}\sigma'_{xx} - i\sigma''_{xx}\sigma'_{zz} + \sigma''_{xx}\sigma''_{zz}}\right) = 0. \tag{34}$$

For a lossless surface, $\sigma'_{xx} = \sigma'_{zz} = 0$, leading to

$$\mathrm{Im}(iq_z\sqrt{\sigma''_{xx}\sigma''_{zz}}) = 0 \tag{35}$$

such that if $\sigma''_{xx}\sigma''_{zz} > 0$, the BC is along $\mathrm{Im}(q_z)$, and if $\sigma''_{xx}\sigma''_{zz} < 0$, the BC is along $\mathrm{Re}(q_z)$, in agreement with the numerically determined contours.

The branch-cut integrals can be viewed as a continuous superposition of modes. The BP q_z^{TM} is associated with the pair $(q_x, q_z) = (0, q_z^{\mathrm{TM}}) = (0, 9.3)k$ for the numerical example considered), and along the branch cut, as $\mathrm{Re}(q_z)$ increases, $\mathrm{Re}(q_x) = \mathrm{Re}(q_{xp})$ also increases from zero, and the resulting continuum summation of pair values synthesis the beam. Similar comments apply to the branch cut between

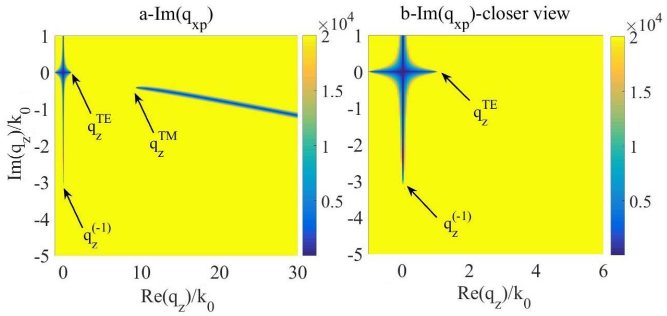

Fig. 7. Branch-cut contours $\mathrm{Im}(q_{xp}) = 0$ determined from a plot of the absolute value of $\mathrm{Im}(q_{xp})$ for a lossy model of a graphene strip array at 10 THz with $\sigma_{xx} = 0.02 + 0.57i$ mS and $\sigma_{zz} = 0.02 - 0.57i$ mS.

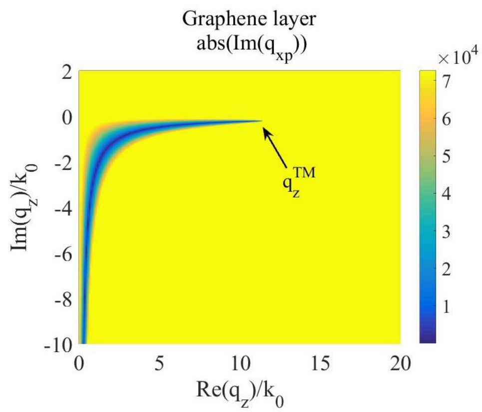

Fig. 8. Branch-cut contour $\mathrm{Im}(q_{xp}) = 0$ determined from a plot of the absolute value of $\mathrm{Im}(q_{xp})$ for graphene with $\mu_c = 0.5$ eV at $T = 0$ K and $f = 20$ THz.

q_z^{TE} and q_z^{-1} (between $q_z = 1.005k$ and $-3.22ik$ in the numerical example considered).

The lossy case is shown in Fig. 7; the branch cut trajectory deflects a bit from the lossless case, but for low-loss surface, the lossless BC contour is sufficient.

As a common special case, for an inductive isotropic surface such as graphene in the far-infrared

$$\sigma_{xx} = \sigma_{zz} = \frac{-ie^2 k_B T}{\pi\hbar^2(\omega - i2\Gamma)} \times \left(\frac{\mu_c}{k_B T} + 2\ln\left(1 + e^{-\frac{\mu_c}{k_B T}}\right)\right). \tag{36}$$

Here, we consider graphene at $T = 300$ K, $\mu_c = 0.5$ eV, and $f = 20$ THz. In this case, the TE related branch point is at $q_z^{\mathrm{TE}} = k(1.0039 + 0.0001i)$, and so is not implicated in the lower half-plane closure, consistent with the surface being inductive (no TE mode is supported). Since only TM branch points occur, only a TM mode exists, and the TM-related BP occurs at $q_z^{\mathrm{TM}}/k = (11.3706 - 0.2088i)$. The two other type-1 branch points move to infinity as the surface becomes isotropic, and therefore, the branch cut extends down the entire imaginary axis (therefore, for both the isotropic and anisotropic cases, there is a branch cut between q_z^{TM} and q_z^{-1}). Fig. 8 shows a surface plot of $\mathrm{Im}(q_{xp})$ in the $q_z -$ plane.

For isotropic and inductive graphene, only a TM mode can propagate, and so the contribution is from the TM-related branch point and associated cut, as expected. For the graphene strip array anisotropic case, the hybrid nature of the modes supported by such a surface involve both TE and TM-related branch points, and in contrast to the isotropic case, three branch points contribute to the field.

G. Conductivity and Its Effect on Branch Points and SPP Confinement

Analytically, it can be shown that both type-1 branch points $q_z^{(\pm 1)}$ can be connected to a TE or TM branch point, depending on the conductivity value. Two cases are of particular interest, small conductivity values, $(\mathrm{Im}(\sigma_{xx/zz})\eta)^2 \ll 1$, and large conductivity values, $(\mathrm{Im}(\sigma_{xx/zz})\eta)^2 \gg 1$. For small conductivity values, from (28) and (29), we have

$$q_z^{TM} = k\sqrt{1 - \left(\frac{2}{\eta\sigma_{zz}}\right)^2} \longrightarrow (\eta\sigma_{zz})^2 = \frac{4}{1 - \left(\frac{q_z^{\mathrm{TM}}}{k}\right)^2} \tag{37}$$

$$q_z^{TE} = k\sqrt{1 - \left(\frac{\eta\sigma_{xx}}{2}\right)^2} \longrightarrow \frac{1}{(\eta\sigma_{xx})^2} = \frac{1}{4}\frac{1}{1 - \left(\frac{q_z^{\mathrm{TE}}}{k}\right)^2}. \tag{38}$$

Making these replacements in (30) and (31) and using the fact that for small conductivity like in our previous numeric example ($\sigma_{xx} = 0.02 + 0.57i$ mS and $\sigma_{zz} = 0.02 - 0.57i$ mS), we have $(\mathrm{Im}(\sigma_{xx/zz})\eta)^2 \ll 1$, and then, $|q_z^{\mathrm{TM}}| \gg k$ and $|q_z^{\mathrm{TE}}| \approx k$, and so $|q_z^{\mathrm{TE}}|^2 \ll |q_z^{\mathrm{TM}}|^2$, such that

$$q_z^{(\pm 1)} = \frac{k}{2}\sqrt{\frac{1}{1 - \left(\frac{q_z^{\mathrm{TE}}}{k}\right)^2}\frac{\sigma_{xx} \mp 2\sigma_{xx}}{\sigma_{zz} - \sigma_{xx}}}. \tag{39}$$

Therefore, for small values of σ_{xx} and σ_{zz}, the type-1 branch points are governed by (and associated with) the TE branch point q_z^{TE}.

For larger values of σ_{xx} and σ_{zz}, the situation is different. In this case, for $(\mathrm{Im}(\sigma_{xx/zz})\eta)^2 \gg 1$, we have $|q_z^{\mathrm{TM}}|^2 \ll |q_z^{\mathrm{TE}}|^2$ and it can be shown that an approximate expression for the type-1 branch point is (39) with q_z^{TM} replacing q_z^{TE}; the type-1 branch points are associated with the TM-related branch point. As the conductivity changes from a small to a large value, q_z^{TE} and q_z^{TM} move toward each other and then cross, and eventually interchange roles. Setting (28) and (29) equal to each other, it can be shown that these type-0 branch points meet at a frequency, such that $\sigma_{xx}\sigma_{zz} = 4/\eta^2$.

As an example of a large conductivity situation, conductivity tensor components $\sigma_{xx} = 1.3 + 16.9i$ mS and $\sigma_{zz} = 0.4 - 9.2i$ mS are attainable using multilayer graphene to form the strip array. For this set of conductivities, the branch points and the branch cuts are shown in Fig. 9. As can be seen, q_z^{TE} exceeds q_z^{TM}, there is a branch cut from q_z^{TE} to infinity, a branch cut between q_z^{TM} and q_z^{-1}, and q_z^{-1} is connected to q_z^{TM}.

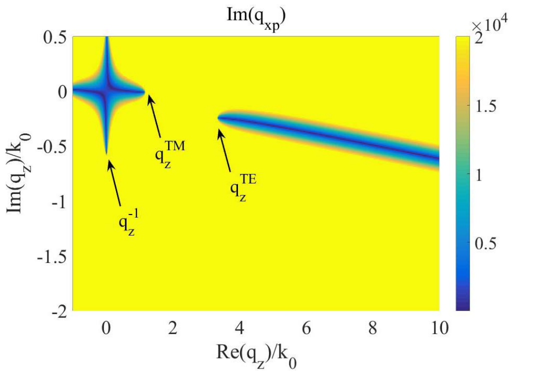

Fig. 9. Branch-cut contours $\mathrm{Im}(q_{xp}) = 0$ determined from a plot of the absolute value of $\mathrm{Im}(q_{xp})$ for a lossy model of multilayer graphene strip at 10 THz, $\sigma_{xx} = 1.3 + 16.9i$ mS, and $\sigma_{zz} = 0.4 - 9.2i$ mS.

VI. Directive SPPs on Hyperbolic and Anisotropic Surfaces

A. Anisotropic Hyperbolic Layer (Graphene Strip Array)

As shown in Appendix A, conductivity components $\sigma_{xx} = 0.02 + 0.57i$ mS and $\sigma_{zz} = 0.02 - 0.57i$ mS can be realized using an array of graphene strips with $\mu_c = 0.33$ eV, strip width $W = 59$ nm, and period $L = 64$ nm. For this anisotropic hyperbolic surface, Fig. 10(a) shows the electric field E_y, the dominant field component, computed as a real-line integral (32), and as a sum of branch cut integrals (33); excellent agreement is found between the two methods (the branch-cut integrals are faster to compute than the brute-force numerical integrals, but no attempt was made to optimize either integration). The branch cuts for this case are shown in Fig. 7. Fig. 10(b) and (c) shows similar agreement for different strip configurations as discussed in the following.

Although the direction of the beam is electronically controllable via the chemical potential, different combinations of physical parameters of the graphene strip array (width W and periodicity L) can also be used to produce a desired beam. An optimum geometry to produce a beam in a certain direction can be found by tuning all of these parameters simultaneously.

From (22), in the hyperbolic regime, propagation along a desired direction can be obtained if the tensor conductivity components have the proper ratio. Designing a hyperbolic metasurface to produce a beam in a desired direction (e.g., choosing the strip width and period) can be done by trial-and-error tuning of all geometrical and electrical parameters of the system, but a multivariable optimization, such as a genetic algorithm (GA) is a good choice for this task [48], [49]. Ideally, the physical layout of the metasurface (graphene strips in the case) should be designed so that the effective (homogenized) conductivity tensor elements are hyperbolic, and have large imaginary part and small real part, since such a surface can support a well-confined, long-range SPP. Here, we used the cost function to be minimized as

$$\begin{aligned}\Psi(L, W, \mu_c, \phi) &= \alpha(\mathrm{Re}(\sigma_{xx}) + \mathrm{Re}(\sigma_{zz})) \\ &\quad + \frac{\beta}{|\mathrm{Im}(\sigma_{xx})| + |\mathrm{Im}(\sigma_{zz})|} + \gamma\left(\tan^2(\phi) + \frac{\sigma_{zz}}{\sigma_{xx}}\right) \quad (40)\end{aligned}$$

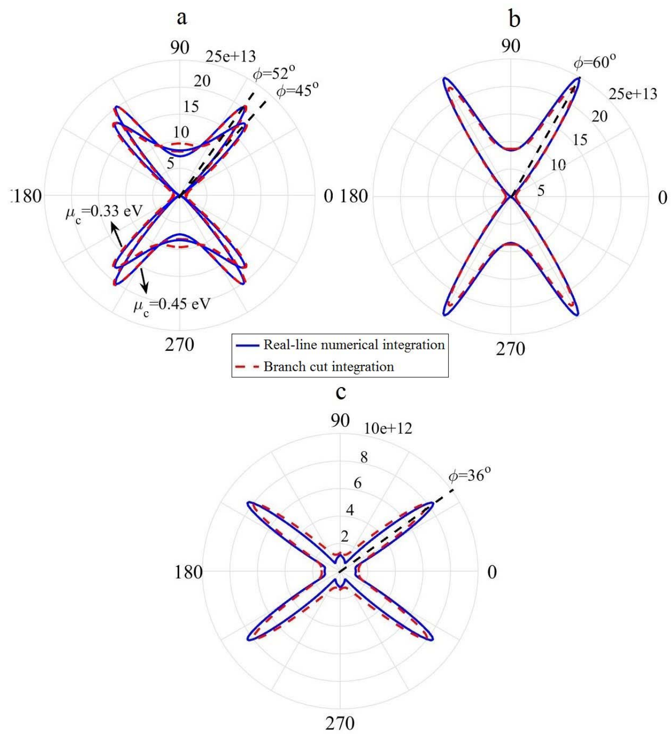

Fig. 10. Electric field E_y excited by a y-directed dipole current above a graphene strip array. (a) Graphene with $\mu_c = 0.45$ eV, $\mu_c = 0.33$ eV, $W = 59$ nm, $L = 64$ nm, $\sigma_{xx} = 0.02+0.57i$ mS, and $\sigma_{zz} = 0.02-0.57i$ mS. (b) $\mu_c = 0.45$ eV, $W = 56.1$ nm, $L = 62.4$ nm, $\sigma_{xx} = 0.003+0.25i$ mS, and $\sigma_{zz} = 0.03-0.76i$ mS. (c) Strip array with a five-layer graphene, $\mu_c = 1$ eV, $W = 196$ nm, $L = 200$ nm, $\sigma_{xx} = 1.3+16.9i$ mS, and $\sigma_{zz} = 0.4-9.2i$ mS. Blue line: integration along the real axis (32). Dashed red line: integration along the branch cuts (33). $f = 10$ THz, $\rho = 0.2\lambda$, and $y = 0.005\lambda$.

where σ_{xx} and σ_{zz} are defined in (41) in Appendix A. The cost function in (40) is a multiobjective cost function and the coefficients α, β, and γ assign a weight (0 to 1) to each objective regarding to its importance. The first term in (40) assures a small real part of conductivity, the second term assures a large imaginary part, and the last term assures the correct ratio for σ_{zz} and σ_{xx} to obtain the SPP beam in desired direction specified by ϕ. It was found that $\alpha = 0.2$ and $\beta = \gamma = 0.4$ lead to good results.

The physical strip geometry leading to the beam in Fig. 10(a) was found in this manner, for a specified beam angle of 45°. Note the excellent agreement between desired and obtained beam angle. The chemical potential was then changed to produce the beam at 52°, for a fixed geometry. Thus, a significant aspect of using a graphene strip array is its electronic tunability by, e.g., varying the bias to control the chemical potential.

In Fig. 10(b), a desired beam angle of 60° was sought, and the GA was used to determine the optimized parameters; $\mu_c = 0.45$ eV, $W = 56.1$ nm, and $L = 62.4$ nm, such that $\sigma_{xx} = 0.003+0.25i$ mS and $\sigma_{zz} = 0.03-0.76i$ mS, leading to the desired beam. Again, excellent agreement is found between the desired and final beam angles.

As a final example for the graphene strip array, Fig. 10(c) shows E_y for the case of multilayer graphene strips (to increase the conductivity). By using five layers of graphene with $\mu_c = 1$ eV,

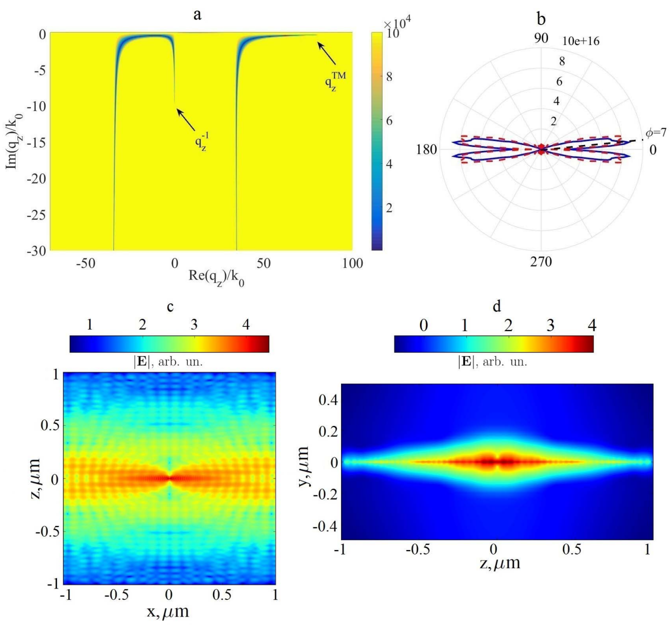

Fig. 11. (a) Branch-cut contours for $\mathrm{Im}(q_{xp}) = 0$ determined from the absolute value of $\mathrm{Im}(q_{xp})$ in the q_z plane. (b) Absolute value of E_y excited by a y-directed dipole current source above BP with doping level $10 \times 10^{13}/\mathrm{cm}^2$ at $f = 92.6$ THz. Blue line: integration along the real axis (32). Dashed red line: integration along the branch cuts (33). $\rho = 0.2\lambda$ and $y = 0.005\lambda$. (c) SPP field in-plane distribution in the logarithmic scale calculated by FDTD. (d) SPP field vertical variation in the logarithmic scale calculated by FDTD.

$W = 196$ nm, and $L = 200$ nm, the conductivities are $\sigma_{xx} = 1.3 + 16.9i$ mS and $\sigma_{zz} = 0.4 - 9.2i$ mS. The branch cuts are shown in Fig. 9. For this case, (22) indicates that the beam should be directed along $\phi = 36°$. Again, excellent agreement is found between the two methods and the position of the beam is along the desired angle.

B. Anisotropic Nonhyperbolic Layer (Black Phosphorus)

As discussed in Appendix B, BP is a natural material that can be used as a platform to realize an anisotropic surface. Although BP exhibits a hyperbolic regime, the resulting values of conductivity are rather small (to produce a hyperbolic response the interband conductivity must dominate one of the conductivity values (σ_{xx} or σ_{zz}), and the intraband conductivity must dominate the other component, resulting in the required sign difference). Although a hyperbolic SPP can be excited, the residue is not generally the dominant response. Therefore, in order to consider larger values of BP conductivity, we consider the nonhyperbolic (Drude) regime. A 10-nm-thick BP film with doping level $10 \times 10^{13}/\mathrm{cm}^2$ has conductivity tensor components $\sigma_{xx} = 0.0008 - 0.2923i$ mS and $\sigma_{zz} = 0.0002 - 0.0658i$ mS at $f = 92.6$ THz. Using (28), (29), and (31), a surface with these conductivity components has $q_z^{\mathrm{TM}} = k(80.6804 - 0.2114i)$, $q_z^{\mathrm{TE}} \approx k$, and $q_z^{(-1)} = k(-0.0300 - 10.3165i)$.

The imaginary components of the conductivities are negative, so that the surface is not able to support TE modes (the TE branch point is located at the upper half of the q_z plane, and so not captured for $z - z' > 0$). The only active branch points are the TM-related branch point and $q_z^{(-1)}$. Fig. 11(a) shows the branch points and associated branch cuts in the q_z plane. One important difference between branch cuts in this case and in the previous hyperbolic cases is the branch cut trajectory. From (35) for the hyperbolic case, because of the condition $\mathrm{Im}(\sigma_{xx})\mathrm{Im}(\sigma_{zz}) < 0$, the branch cut trajectory was along the real axis, but for the anisotropic nonhyperbolic case, we have $\mathrm{Im}(\sigma_{xx})\mathrm{Im}(\sigma_{zz}) > 0$ and so the trajectory for large q_z is parallel to the imaginary axis.

As shown in Fig. 11(b), this anisotropic nonhyperbolic surface can support a directed SPP, although the beam is directed primarily along one of the coordinate axes. The electric field computed as a real-line integral (32) is in good agreement with the electric field obtained as a sum of branch cut integrals (33). Fig. 11(c) shows the SPP field in the logarithmic scale calculated by numerically solving Maxwell's equations using a commercial finite-difference time-domain method (FDTD) from Lumerical solutions [45]. Good agreement with the results obtained by complex plane analysis is observed. Fig. 11(d) shows the vertical variation of the beam in the logarithmic scale calculated by Lumerical, showing strong SPP confinement to the surface. Using Green's function the attenuation length was found to be $p = \lambda/12\pi$.

VII. Conclusion

We have studied the electromagnetic response of 2-D anisotropic and hyperbolic surfaces and developed a method (based on complex plane analysis) for the efficient computation of electric field excited on such surfaces. A solution in term of electric field Sommerfeld integrals has been obtained for the electromagnetic field due to a vertical dipole current source located in close proximity to the surface. Poles, branch points, and related branch cuts and their relative importance and physical meaning for surface wave propagation have been emphasized. A first-order approximation has also been obtained using the SP method. Examples have been shown for a graphene strip array and BP.

Appendix A
Graphene Strip Hyperbolic Metasurface

A schematic of an array of graphene strips is shown in Fig. 12(a). This densely packed strip surface can act as a physical implementation of a metasurface at terahertz and near-infrared frequencies [3], [46]. The dispersion topology of the proposed structure may range from elliptical to hyperbolic as a function of its geometrical and electrical parameters. The in-plane effective conductivity tensor of the proposed structure can be analytically obtained using an effective medium theory as [3]

$$\sigma_{zz}^{\mathrm{eff}} = \sigma\frac{W}{L} \quad \text{and} \quad \sigma_{xx}^{\mathrm{eff}} = \frac{L\sigma\sigma_c}{W\sigma_c + G\sigma} \tag{41}$$

where L and W are the periodicity and width of the strips, respectively, $G = L - W$ is the separation distance between two consecutive strips, σ is graphene conductivity (36), and $\sigma_c = j(\omega\epsilon_0 L/\pi)\ln(\csc(\pi G/2L))$ is an equivalent conductivity associated with the near-field coupling between adjacent strips obtained using an electrostatic approach [47]. These effective parameters are valid only when the homogeneity condition $L \ll \lambda_{\mathrm{SPP}}$ is satisfied, where λ_{SPP} is

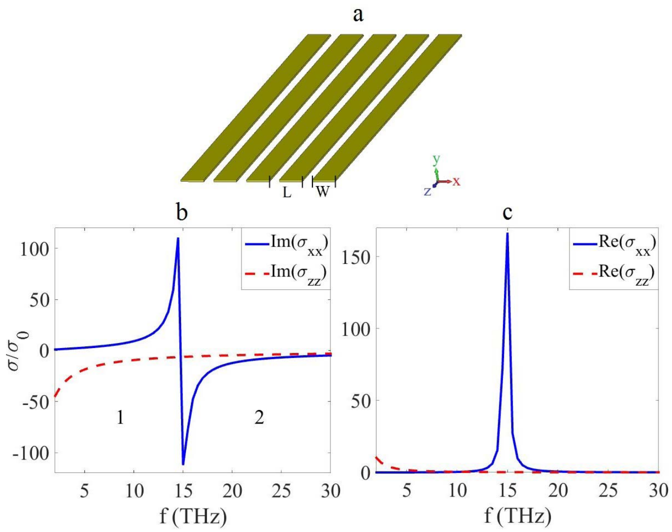

Fig. 12. (a) Array of graphene strips. (b) Imaginary parts of σ_{xx} and σ_{zz} and (c) real parts of σ_{xx} and σ_{zz} normalized to $\sigma_0 = e^2/4\hbar$ for a graphene strip array with $\tau = 0.35$ ps, $\mu_c = 0.33$ eV, $W = 59$ nm, and $L = 64$ nm. Region 1 is hyperbolic and region 2 is simply anisotropic.

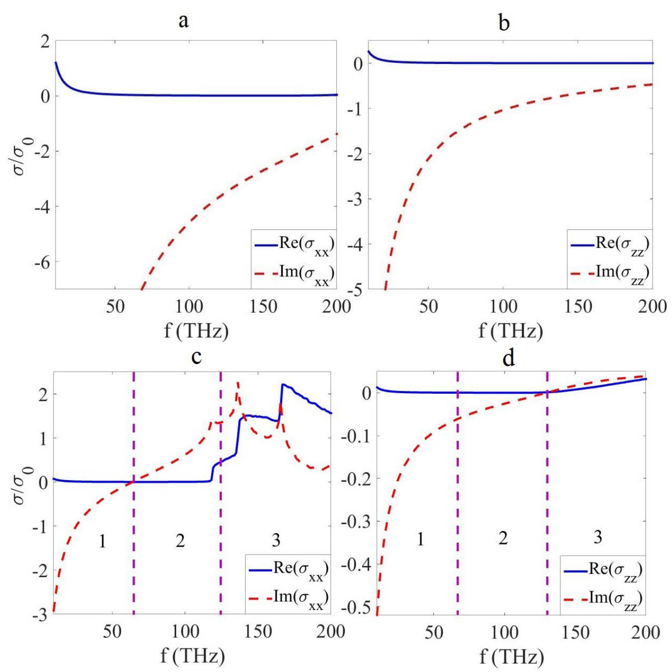

Fig. 13. Real and imaginary parts of σ_{xx} and σ_{zz} (x and z are in-plane crystal axes of BP, with x along the small effective mass direction, or commonly called the armchair direction) obtained at doping level (a) and (b) $10 \times 10^{13}/\text{cm}^2$ and (c) and (d) $5 \times 10^{12}/\text{cm}^2$ normalized to $\sigma_0 = e^2/4\hbar$ with a 10 nm thickness. Regions 1 and 3 show anisotropic inductive and capacitive responses, respectively, and region 2 shows the hyperbolic regime. $T = 300$ K and damping is 2 meV.

the plasmon wavelength in the in-plane direction perpendicular to the strips (x in this case), thus leading to a homogeneous 2-D metasurface. Fig. 12(b) and (c) shows σ_{xx} and σ_{zz} in a wide range of frequency for a graphene strip array with graphene parameters $\tau = 0.35$ ps, $\mu_c = 0.33$ eV, and geometrical parameters $W = 59$ nm and $L = 64$ nm. As can be seen in Fig. 12(b), this structure can exhibit a hyperbolic response, as well as implement a nonhyperbolic although anisotropic surface.

Appendix B
Black Phosphorus

BP is an anisotropic monolayer or thin-film material that can support surface plasmons [50]. Fig. 13 shows the in-plane conductivity tensor components at two doping levels, $10 \times 10^{13}/\text{cm}^2$ and $5 \times 10^{12}/\text{cm}^2$, obtained from a Kubo formula as described in [23]. For a 10-nm BP film, the electronic bandgap is approximately 0.5 eV. This accounts for the observed interband absorption along the x polarization, and also characterized by weak interband absorption along z.

It can be seen that by increasing the doping level, larger conductivity components are attainable but the hyperbolic region is also pushed toward higher frequencies. In Fig. 13(a) and (b), BP is an inductive anisotropic (nonhyperbolic) surface, while in Fig. 13(c) and (d), regions 1 and 3 show anisotropic inductive and capacitive responses, respectively, and region 2 shows the anisotropic hyperbolic region.

Acknowledgment

The authors would like to thank the reviewers for their careful consideration and suggestions.

References

[1] V. P. Drachev, V. A. Podolskiy, and A. V. Kildishev, "Hyperbolic metamaterials: New physics behind a classical problem," *Opt. Exp.*, vol. 21, no. 12, pp. 15048–15064, 2013.
[2] M. A. K. Othman, C. Guclu, and F. Capolino, "Graphene-based tunable hyperbolic metamaterials and enhanced near-field absorption," *Opt. Exp.*, vol. 21, no. 6, pp. 7614–7632, 2013.
[3] J. S. Gomez-Diaz, M. Tymchenko, and A. Alù, "Hyperbolic plasmons and topological transitions over uniaxial metasurfaces," *Phys. Rev. Lett.*, vol. 114, no. 23, p. 233901, 2015.
[4] V. A. Podolskiy and E. E. Narimanov, "Strongly anisotropic waveguide as a nonmagnetic left-handed system," *Phys. Rev. B*, vol. 71, no. 20, p. 201101, 2005.
[5] A. A. Govyadinov and V. A. Podolskiy, "Metamaterial photonic funnels for subdiffraction light compression and propagation," *Phys. Rev. B*, vol. 73, p. 155108, Apr. 2006.
[6] J. Yao, X. Yang, X. Yin, G. Bartal, and X. Zhang, "Three-dimensional nanometer-scale optical cavities of indefinite medium," *Proc. Nat. Acad. Sci. USA*, vol. 108, no. 28, pp. 11327–11331, 2011.
[7] E. F. Kuester, M. A. Mohamed, M. Piket-May, and C. L. Holloway, "Averaged transition conditions for electromagnetic fields at a metafilm," *IEEE Trans. Antennas Propag.*, vol. 51, no. 10, pp. 2641–2651, Oct. 2003.
[8] N. Yu and F. Capasso, "Flat optics with designer metasurfaces," *Nature Mater.*, vol. 13, pp. 139–150, Jan. 2014.
[9] K. S. Novoselov *et al.*, "Two-dimensional atomic crystals," *Proc. Nat. Acad. Sci. USA*, vol. 102, no. 103, pp. 10451–10453, 2005.
[10] T. Low and P. Avouris, "Graphene plasmonics for terahertz to mid-infrared applications," *ACS Nano*, vol. 8, no. 2, pp. 1086–1101, 2014.
[11] F. H. L. Koppens, D. E. Chang, and F. J. García de Abajo, "Graphene plasmonics: A platform for strong light–matter interactions," *Nano Lett.*, vol. 11, no. 8, pp. 3370–3377, 2011.
[12] G. W. Hanson, "Dyadic Green's functions and guided surface waves for a surface conductivity model of graphene," *J. Appl. Phys.*, vol. 103, no. 6, p. 064302, 2008.
[13] F. J. García de Abajo, "Graphene plasmonics: Challenges and opportunities," *ACS Photon.*, vol. 1, no. 3, pp. 135–152, Feb. 2014.
[14] E. Forati, G. W. Hanson, A. B. Yakovlev, and A. Alù, "Planar hyperlens based on a modulated graphene monolayer," *Phys. Rev. B*, vol. 89, no. 8, p. 081410, Feb. 2014.
[15] G. W. Hanson, S. A. H. Gangaraj, C. Lee, D. G. Angelakis, and M. Tame, "Quantum plasmonic excitation in graphene and loss-insensitive propagation," *Phys. Rev. A*, vol. 92, p. 013828, Jul. 2015.

[16] D. L. Sounas *et al.*, "Faraday rotation in magnetically biased graphene at microwave frequencies," *Appl. Phys. Lett.*, vol. 102, no. 19, p. 191901, 2013.
[17] A. Vakil and N. Engheta, "Transformation optics using graphene," *Science*, vol. 332, no. 6035, pp. 1291–1294, 2011.
[18] A. Morita, "Semiconducting black phosphorus," *Appl. Phys. A*, vol. 39, no. 4, pp. 227–242, Apr. 1986.
[19] L. Li *et al.*, "Black phosphorus field-effect transistors," *Nature Nanotechnol.*, vol. 9, pp. 372–377, Mar. 2014.
[20] H. Liu *et al.*, "Phosphorene: An unexplored 2D semiconductor with a high hole mobility," *ACS Nano*, vol. 8, no. 4, pp. 4033–4041, 2014.
[21] F. Xia, H. Wang, and Y. Jia, "Rediscovering black phosphorus as an anisotropic layered material for optoelectronics and electronics," *Nature Commun.*, vol. 5, p. 4458, Jul. 2014.
[22] S. P. Koenig, R. A. Doganov, H. Schmidt, A. H. Neto, and B. Özyilmaz, "Electric field effect in ultrathin black phosphorus," *Appl. Phys. Lett.*, vol. 104, no. 10, p. 103106, 2014.
[23] T. Low *et al.*, "Tunable optical properties of multilayer black phosphorus thin films," *Phys. Rev. B*, vol. 90, no. 7, p. 075434, 2014.
[24] V. Tran, R. Soklaski, Y. Liang, and L. Yang, "Layer-controlled band gap and anisotropic excitons in few-layer black phosphorus," *Phys. Rev. B*, vol. 89, no. 23, p. 235319, 2014.
[25] J. Qiao, X. Kong, Z.-X. Hu, F. Yang, and W. Ji, "High-mobility transport anisotropy and linear dichroism in few-layer black phosphorus," *Nature Commun.*, vol. 5, p. 4475, Jul. 2014.
[26] T. Low, M. Engel, M. Steiner, and P. Avouris, "Origin of photoresponse in black phosphorus phototransistors," *Phys. Rev. B*, vol. 90, no. 8, p. 081408, 2014.
[27] M. Engel, M. Steiner, and P. Avouris, "Black phosphorus photodetector for multispectral, high-resolution imaging," *Nano Lett.*, vol. 14, no. 11, pp. 6414–6417, 2014.
[28] M. Buscema *et al.*, "Fast and broadband photoresponse of few-layer black phosphorus field-effect transistors," *Nano Lett.*, vol. 14, no. 6, pp. 3347–3352, 2014.
[29] H. Yuan *et al.*, "Polarization-sensitive broadband photodetector using a black phosphorus vertical p–n junction," *Nature Nanotechnol.*, vol. 10, pp. 707–713, Jun. 2015.
[30] N. Youngblood, C. Chen, S. J. Koester, and M. Li, "Waveguide-integrated black phosphorus photodetector with high responsivity and low dark current," *Nature Photon.*, vol. 9, pp. 247–252, Mar. 2015.
[31] A. Castellanos-Gomez *et al.*, "Isolation and characterization of few-layer black phosphorus," *2D Mater.*, vol. 1, no. 2, p. 025001, 2014.
[32] O. Y. Yermakov, A. I. Ovcharenko, M. Song, A. A. Bogdanov, I. V. Iorsh, and Y. S. Kivshar, "Hybrid waves localized at hyperbolic metasurfaces," *Phys. Rev. B*, vol. 91, no. 23, p. 235423, 2015.
[33] A. Nemilentsau, T. Low, and G. W. Hanson, "Anisotropic 2D materials for tunable hyperbolic plasmonics," *Phys. Rev. Lett.*, vol. 116, no. 6, p. 066804, 2016.
[34] J. Kong, *Electromagnetic Wave Theory*. New York, NY, USA: Wiley, 1986.
[35] D. C. Chang and E. F. Kuester, "An analytic theory for narrow open microstrip," *Arch. Elek. Ubertragungstech.*, vol. 33, pp. 199–206, 1979.
[36] J. S. Bagby, C.-H. Lee, D. P. Nyquist, and Y. Yuan, "Identification of propagation regimes on integrated microstrip transmission lines," *IEEE Trans. Microw. Theory Techn.*, vol. 41, no. 11, pp. 1887–1894, Nov. 1993.
[37] D. P. Nyquist and D. J. Infante, "Discrete higher-order leaky-wave modes and the continuous spectrum of stripline," *IEICE Trans.*, vol. E78-C, no. 10, pp. 1331–1338, Oct. 1995.
[38] D. P. Nyquist, J. M. Grimm, D. J. Infante, and H. Braunisch, "Classification of the proper propagation-mode spectrum and leaky-wave modes on open planar waveguides," *Electromagnetics*, vol. 17, no. 2, pp. 105–130, 1997.
[39] A. Ishimaru, *Electromagnetic Wave Propagation, Radiation, and Scattering*. Englewood Cliffs, NJ, USA: Prentice-Hall, 1991.
[40] F. Liang, A. B. Yakovlev, and G. W. Hanson, "Optimum surface plasmon excitation and propagation on conductive two-dimensional materials and thin films," *IEEE Trans. Antennas Propag.*, vol. 63, no. 4, pp. 1765–1774, Apr. 2015.
[41] L. B. Felsen and N. Marcuvitz, *Radiation and Scattering of Waves*. London, U.K.: Oxford Univ. Press, 1994.
[42] H. L. Bertoni and A. Hessel, "Ray description for point source excited surface waves in stratified anisotropic media," *Radio Sci.*, vol. 4, no. 1, pp. 73–81, 1969.
[43] A. R. Forsyth, *Theory of Functions of a Complex Variable*. Cambridge, U.K.: Cambridge Univ. Press, 1893.
[44] G. W. Hanson and A. B. Yakovlev, "An analysis of leaky-wave dispersion phenomena in the vicinity of cutoff using complex frequency plane singularities," *Radio Sci.*, vol. 33, no. 4, pp. 803–820, Jul./Aug. 1998.
[45] *Lumerical Solutions*. [Online]. Available: http://www.lumerical.com/tcad-products/fdtd/
[46] O. V. Shapoval, J. S. Gomez-Diaz, J. Perruisseau-Carrier, J. R. Mosig, and A. I. Nosich, "Integral equation analysis of plane wave scattering by coplanar graphene-strip gratings in the THz range," *IEEE Trans. THz Sci. Technol.*, vol. 3, no. 5, pp. 666–674, Sep. 2013.
[47] C. S. R. Kaipa, A. B. Yakovlev, G. W. Hanson, Y. R. Padooru, F. Medina, and F. Mesa, "Enhanced transmission with a graphene-dielectric microstructure at low-terahertz frequencies," *Phys. Rev. B*, vol. 85, p. 245407, Jun. 2012.
[48] R. L. Haupt, "An introduction to genetic algorithms for electromagnetics," *IEEE Antennas Propag. Mag.*, vol. 37, no. 2, pp. 7–15, Apr. 1995.
[49] R. L. Haupt and D. H. Werner, *Genetic Algorithms in Electromagnetics*. Hoboken, NJ, USA: Wiley, 2007.
[50] T. Low *et al.*, "Plasmons and screening in monolayer and multilayer black phosphorus," *Phys. Rev. Lett.*, vol. 113, no. 10, p. 106802, 2014.

Seyyed Ali Hassani Gangaraj (S'15) was born in Iran, in 1988. He received the B.Sc. and M.Sc. degrees in electrical engineering from the Iran University of Science and Technology (IUST), Tehran, Iran, in 2010 and 2012, respectively. He is currently pursuing the Ph.D. degree in electrical engineering, applied electromagnetics with the University of Wisconsin–Milwaukee (UWM), Milwaukee, WI, USA.

He was a Research Assistant with the Microwave Engineering Laboratory, IUST. He is currently a Research and Teaching Assistant with UWM. His current research interests include plasmonics, metamaterials, quantum plasmonics, and photonic topological insulators.

Mr. Hassani Gangaraj is a Technical Reviewer of the IEEE TRANSACTIONS ON ANTENNAS AND PROPAGATION and the *Optics Express* (Optical Society of America journals).

Tony Low received the Ph.D. degree from the National University of Singapore, Singapore, in 2008.

Previously, he was an in-house theorist with various experimental groups, Columbia University, New York, NY, USA, Yale University, New Haven, CT, USA, and IBM Thomas J. Watson Research Center, Yorktown Heights, NY, USA. While at IBM, from 2011 to 2014, he served as an Industry Liaison to various universities under the Nanoelectronics Research Initiative with the goal of finding the next electronics switch. He currently leads the Theory And Computational Nanoscience Group with the Department of Electrical and Computer Engineering, University of Minnesota, Minneapolis, MN. USA.

Dr. Low received the IEEE Electron Device Society Fellowship in 2005, the Singapore Millennium Fellowship in 2007, the KITP Rice Family Fund Fellowship in 2012, the IBM Invention Award in 2013, and the IBM Pat Goldberg Memorial Best Paper Award in 2014.

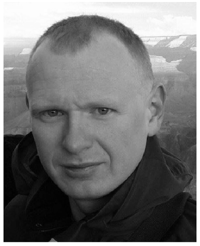

Andrei Nemilentsau was born in Belarus, in 1982. He received the M.Sc. degree in physics and the Ph.D. degree in theoretical physics from Belarusian State University, Minsk, Belarus, in 2004 and 2009, respectively.

He was a Research Associate with the Institute for Nuclear Problems, Belarusian State University from 2009 to 2011, a Post-Doctoral Associate with the Physics Department, Lehigh University, Bethlehem, PA, USA, from 2011 to 2014, and a Visiting Professor with the Department of Electrical Engineering, University of Wisconsin–Milwaukee, Milwaukee, WI, USA, from 2014 to 2016. He is currently a Researcher with the Department of Electrical and Computer Engineering, University of Minnesota, Minneapolis, MN, USA. His current research interests include nanoelectromagnetism, the optical properties of and excitons in 2D materials, plasmonics, metamaterials and metasurfaces, plasmonics, and near-field radiative heat transfer.

George W. Hanson (S'85–M'91–SM'98–F'09) was born in Glen Ridge, NJ, USA, in 1963. He received the B.S.E.E. degree from Lehigh University, Bethlehem, PA, USA, in 1986, the M.S.E.E. degree from Southern Methodist University, Dallas, TX, USA, in 1988, and the Ph.D. degree in electrical engineering from Michigan State University, East Lansing, MI, USA, in 1991.

From 1986 to 1988, he was a Development Engineer with General Dynamics, Fort Worth, TX, USA, where he was involved in radar simulators. From 1988 to 1991, he was a Research and Teaching Assistant with the Department of Electrical Engineering, Michigan State University. He is currently a Professor of Electrical Engineering and Computer Science with the University of Wisconsin–Milwaukee, Milwaukee, WI, USA. He is a coauthor of the book *Operator Theory for Electromagnetics: An Introduction* (Springer, 2002), and the author of *Fundamentals of Nanoelectronics* (Prentice-Hall, 2007). His current research interests include nanoelectromagnetics, plasmonics, quantum optics, and mathematical methods in electromagnetics.

Dr. Hanson is a member of URSI Commission B, Sigma Xi, and Eta Kappa Nu. In 2006, he was a recipient of the S.A. Schelkunoff Best Paper Award from the IEEE Antennas and Propagation Society. He was an Associate Editor of the IEEE TRANSACTIONS ON ANTENNAS AND PROPAGATION from 2002 to 2007.